BNL-212210-2019-JAAM

In Situ Time-Resolved X-ray Scattering Study of Isotactic Polypropylene in Additive Manufacturing

Y. Shmueli, M. Zhernenkov

To be published in "ACS Applied Materials & Interfaces"

September 2019

Photon Sciences

Brookhaven National Laboratory

U.S. Department of Energy

USDOE Office of Science (SC), Basic Energy Sciences (BES) (SC-22)

Notice: This manuscript has been authored by employees of Brookhaven Science Associates, LLC under Contract No. DE-SC0012704 with the U.S. Department of Energy. The publisher by accepting the manuscript for publication acknowledges that the United States Government retains a non-exclusive, paid-up, irrevocable, world-wide license to publish or reproduce the published form of this manuscript, or allow others to do so, for United States Government purposes.

DISCLAIMER

This report was prepared as an account of work sponsored by an agency of the United States Government. Neither the United States Government nor any agency thereof, nor any of their employees, nor any of their contractors, subcontractors, or their employees, makes any warranty, express or implied, or assumes any legal liability or responsibility for the accuracy, completeness, or any third party's use or the results of such use of any information, apparatus, product, or process disclosed, or represents that its use would not infringe privately owned rights. Reference herein to any specific commercial product, process, or service by trade name, trademark, manufacturer, or otherwise, does not necessarily constitute or imply its endorsement, recommendation, or favoring by the United States Government or any agency thereof or its contractors or subcontractors. The views and opinions of authors expressed herein do not necessarily state or reflect those of the United States Government or any agency thereof.

In Situ Time-Resolved X-ray Scattering Study of Isotactic Polypropylene in Additive Manufacturing

Yuval Shmueli,[*,†] Yu-Chung Lin,[†] Sungsik Lee,[‡] Mikhail Zhernenkov,[§] Rina Tannenbaum,[†] Gad Marom,[‡,∥] and Miriam H. Rafailovich[†]

[†]Department of Materials Science and Chemical Engineering, Stony Brook University, Stony Brook, New York 11794, United States

[‡]X-ray Science Division, Argonne National Laboratory, Argonne, Illinois 60349, United States

[§]National Synchrotron Light Source II, Brookhaven National Laboratory, Upton, New York 11973, United States

[∥]Casali Institute of Applied Chemistry, The Institute of Chemistry and the Center for Nanoscience and Nanotechnology, The Hebrew University of Jerusalem, Jerusalem 91904, Israel

ABSTRACT: Using a specially designed apparatus, which collects simultaneous temperature and X-ray scattering data, we performed in situ measurements of the filament during MatEx 3D printing. The data show that the MatEx 3D printing extrusion process provides sufficient shear to form shish-kebab structures, which initially nucleate at the filament surface and spread into the filament core. Time-resolved measurements show that the kebab component near the surface relaxes after deposition of the second filament and enhances chain diffusion across the interface. SEM images indicate near complete interfacial merging of the filaments, which results in excellent mechanical properties.

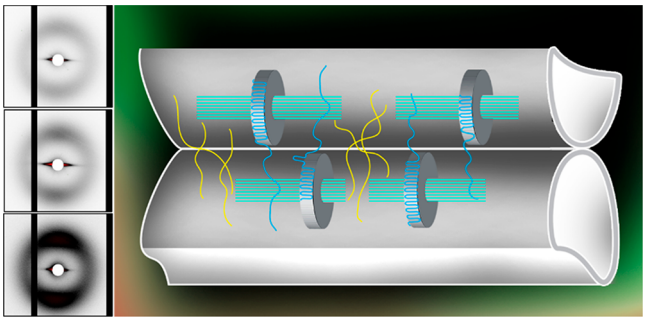

KEYWORDS: *isotactic polypropylene, additive manufacturing, in situ X-ray scattering, shish-kebab, crystallinity*

1. INTRODUCTION

Fused filament fabrication ("FFF"), currently known as Material Extrusion ("MatEx"), is a common form of additive manufacturing, or 3D printing technique, in which a thermoplastic polymer is melted and extruded in specific forms according to the user input file.[1] In contrast to bulk fabrication methods, the MatEx printing process occurs under conditions that are far from equilibrium. In the MatEx process, rather than being extruded or molded in a single operation, structures are built by overlaying multiple layers extruded from a hot moving nozzle. Hence, each layer is initially subjected to high shear and heat as it emerges from the nozzle, and heated again, in the absence of shear, as the nozzle returns to deposit subsequent layers. Hence, the process imposes large thermal and mechanical gradients, which fluctuate rapidly with the movement of the nozzle, and can differ substantially between layers, and even within a single layer, where bulk and surface sections are subject to very different conditions. These factors are especially important when printing with semicrystalline thermoplastic polymers where they determine the crystallization kinetics and the interfacial fusion between filaments, which ultimately determine the mechanical integrity of the printed structure.[2−4] Because these factors are very difficult to predict a priori, and in particular the differences between the surface and the bulk properties, simultaneous in situ imaging of both the thermal gradients and the X-ray scattering profiles during the printing process is essential to understand the structure property relationships of materials produced by this technique.

Here, we describe a set of experiments using polypropylene, a semicrystalline polymer with a high degree of crystallinity, where thermal gradients were monitored using an infrared camera while the crystallinity was mapped in situ using an X-ray microbeam and performing WAXS/SAXS with microscale spatial resolution.

It is well-known that shear influences polymer crystallization.[5,6] Polypropylene is one of the most studied crystalline polymers, where extensive research exists describing the unique morphologies formed as result of applied strain, in comparison to the quiescent condition.[7] In 1965, Peterlin wrote that plastic deformation enhances crystallization.[8] The stretching caused the randomly coiled polymer chains to be oriented. This aligned state is preferable for crystallization not only because it decreases the entropy, but also because it brings the chains to a position from which their inclusion in crystalline structure will not require too much rearrangement. Pennings et al. showed how fibrous crystalline structure can be formed in a polymer solution by crystallization under laminar flow stirring and cooling conditions.[9] Keller et al. showed the steps through which the shear enhances the formation of the crystalline

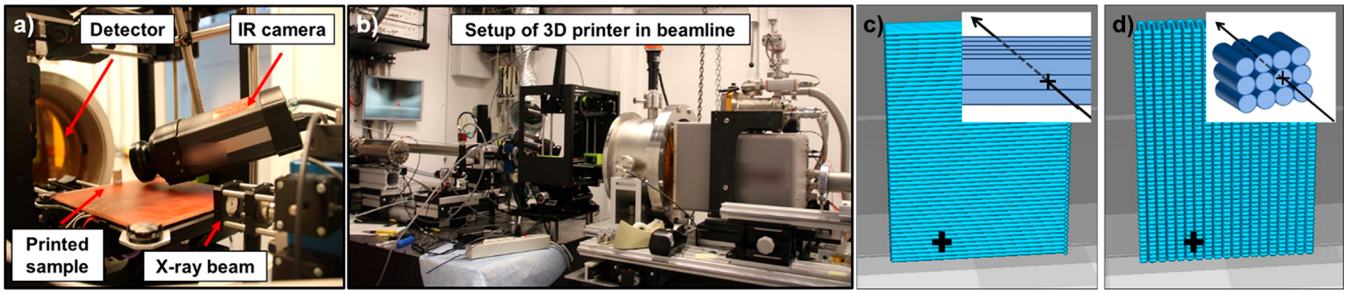

Figure 1. (a) Setup of in situ WAXS and thermal imaging measurements in the beamline. (b) Printer in-line installation. (c,d) In situ WAXS measurements were performed where the structures were irradiated at the position marked with a plus sign, +. The arrow in the inset marks the X-ray beam. Filaments printed perpendicular to the X-ray beam (c) and parallel (d).

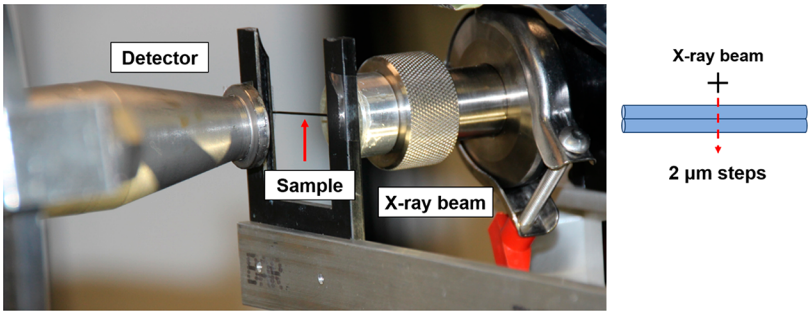

Figure 2. Setup of microbeam SAXS measurements.

structures.[10−12] They introduced the term "row nucleated" describing the first step in which small segments of the sheared polymer made of oriented and stretched chains are the initial nucleation sites. At the second step, these row nucleated sites become connected by the oriented chains into longer fibrous structures known as the "shishs". At the final step, there is the growth of the lamellar structures as disks in radial direction to the shear direction. These disks, known as "kebabs", have a fast growth rate and can rotate in a direction radial to the shear flow. They found that in all of these crystalline structures, the "*c*" direction of the lamellar unit cell, which is also the polymer chain axis, remains oriented parallel to the shear or flow direction. Janeschitz-Kriegl et al. also showed that in shear-induced crystallization first form thread-like nucleation sites followed by crystallization in the lateral direction.[13−15] Comprehensive studies on the shear effect on iPP morphological conformations were done by Kornfield et al.,[16−19] Hsiao et al.,[6,17,18,20−22] and Marom et al.,[5,20,23,24] who introduced synchrotron X-ray scattering as a characterization method to study in situ the effect of induced shear on the shish-kebab formation in iPP and its orientation with the shear direction. Here, we build on these seminal works, and apply the principles toward understanding the internal structures formed during MatEx printing, where polymer flow, shear, and temperature are controlled by the moving nozzle and can fluctuate rapidly with printing geometry. Because the environment during printing is far from equilibrium, these parameters must be accurately measured to model the internal structures and be able to predictably control their quality. We report on the simultaneous use of thermal imaging together with microbeam SAXS/WAXS X-ray scans of iPP filaments during MatEx printing, where we can directly observe the crystallization dynamics and fluctuations as the filaments are being deposited to build the solid structures.

2. MATERIALS AND METHODS

2.1. Materials. Isotactic polypropylene (Mw_{avr} = 250 000, Sigma-Aldrich) pellets were used to produce the samples investigated. Molded samples were produced by compression of the pellets in a Carver hot press at 180 °C, between Kapton sheets, using a stainless-steel mold. Filaments, 3 mm in diameter, were produced from the same pellets, using a Filabot Extruder, with a cooled bed and collected on a spool.

2.2. Methods. *2.2.1. Printing of iPP Samples.* The samples were printed using an Ultimaker Extended 2+ and LulzBot Mini printers. Matlab was used to design the structures and converted into standard G-code for printing. All samples were printed at a nozzle temperature of 230 °C, bed temperature of 60 °C, infill density of 100%, and printing speed of 20 mm/s.

2.2.2. Characterization of Printed Structures. Scanning electron microscopy (SEM) was performed using a LEO1550 Zeiss microscope. Cross-section samples for SEM imaging were prepared by cryo-fracturing. Flexural modulii were measured to evaluate the mechanical properties by three-point bending according to ASTM D790 using DMA Q800, TA Instruments.

2.2.3. Time-Resolved In Situ Wide-Angle X-ray Scattering and Infrared Thermal Imaging Measurements of MatEx Printing. An open-walls "Lulzbot Mini" MatEx printer was placed in beamline 12-BM at the Advanced Photon Source (APS) at Argonne National Laboratory. Samples of dimension 2.5 × 15 × 20 mm^3 were printed in beam, using a nozzle temperature of 230 °C, and the stage temperature was 60 °C, where the thickness was chosen to enable good transmittance and scattering of the X-rays. WAXS measurements at the APS were performed with a beam energy of 16 keV, beam spot size of 500 × 500 μm^2, detector pixels size of 0.146 mm, and detector-to-sample distance of 567 mm. An infrared thermal camera (FLIR, A325sc) with frame rate of 60 Hz, pixel size of 100 μm, detector resolution of 320 × 240, and spectral band of 7.5−13 μm was fixed to monitor the temperature profile during printing of the samples (Figure 1). The thermal imaging was analyzed using ResearchIR software. For polypropylene, the transmission of infrared radiation was calculated by P. T. Tsilingiris,[25] and was found to be at least 40% for films at approximately 0.20 mm, which corresponds roughly to the

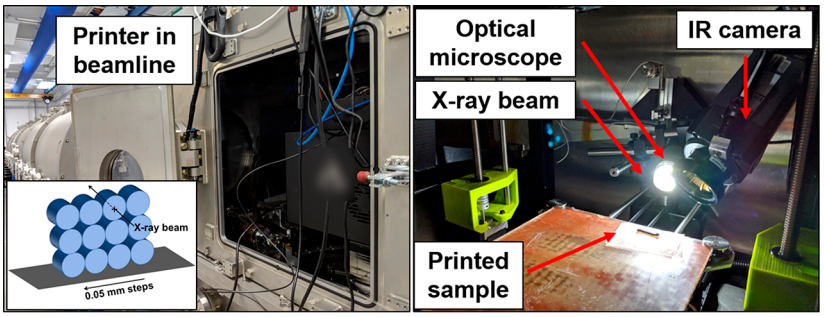

Figure 3. Setup of in situ X-ray microbeam scattering and thermal imaging measurements. Left: Printer installation in beamline (inset: schematic description of measuring mode). Right: Zoomed-in view of measurements setup.

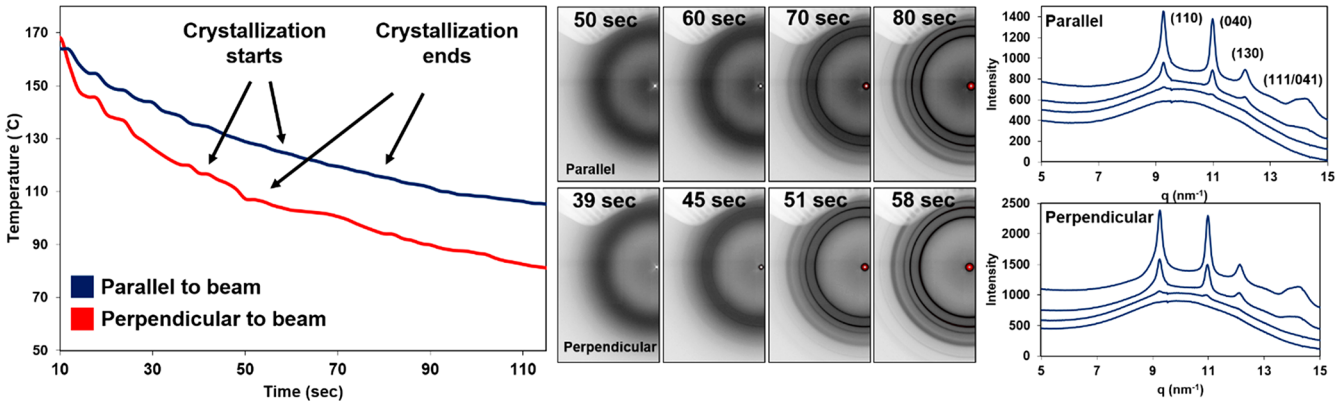

Figure 4. Temperature profile at the measured location at the in situ 3D printing. 2D WAXS patterns with their 1D integrated curves demonstrating the crystallinity evolution at the printed iPP.

radii of the printed filaments, and hence the infrared camera was able to measure the temperatures at the filament core.

X-ray scattering was done in continuous mode of 2 s exposure time. The thermal profile was imaged and recorded continuously. The beam was located at a constant position on the printed sample, and the scattering was measured while the sample was printed and layers were being deposited. Analysis of the scattering data was done by xPolar software.

2.2.4. "Interface-Core" Macrostructure Mapping Using Small-Angle X-ray Scattering Microbeam. Measuring the radial variation in printed filaments crystalline macrostructure was done using a microbeam on beamline 18-ID (BioCAT) in the Advanced Photon Source (APS) at Argonne National Laboratory. The microbeam spot size was $2 \times 20\ \mu m^2$ ($v \times h$) with energy of 12 keV, detector pixels size of 0.172 mm, and detector-to-sample distance of 2030 mm. The samples were placed on a "U" shape metal holder mounted on a 1 μm resolution motor. The setup is shown in Figure 2. Printed structures made of two filaments were placed in a horizontal manner as the beam scanned from the surface to the filaments core in steps of 2 μm. The scanning method used with the beam over the filaments is described in the schematic illustration in Figure 2. Analysis of the scattering data was done by xPolar and MuscleX[26] software.

2.2.5. Time-Resolved Small-\Wide-Angle X-ray Scattering and Infrared Thermal Imaging Using Microbeam. To study the morphological behavior of the printed filaments at the interface between adjacent filaments and at the core, X-ray microbeam was used in situ together with infrared thermal imaging (FLIR, A325sc). Open-walls "Lulzbot Mini" MatEx printer was placed in beamline 12-ID at the NSLS-2 Light Source at Brookhaven National Laboratory (Figure 3). The beam energy was 16 keV with spot size of $2 \times 25\ \mu m^2$ ($v \times h$). Three detectors were used to obtain a wide "q" range: small, medium, and wide angle. The small-angle detector had pixel size of 0.172 mm, detector-to-sample distance of 8287 mm, and acquiring frequency of 10 Hz. The medium range detector had pixel size of 0.109 mm, detector-to-sample distance of 795 mm, and acquiring frequency of 1 Hz. The wide-angle detector had pixel size of 0.172 mm, detector-to-sample distance of 274 mm, and acquiring frequency of 10 Hz. A rectangular shape was printed with dimensions of 2 × 20 × 2.5 mm. The printing was done at a nozzle temperature of 230 °C and a stage temperature of 60 °C. The beam location was adjusted to be at the middle height of the top deposited layer, that is, 0.25 mm from the surface. The beam location was varied at step sizes of 0.05 mm on the lateral movement to have detailed information on the morphological variation. The positional stability of the printer stage was found to be adequate. The beam alignment was monitored before and after each run and found to be stable during the data acquisition time. A schematic description of the measurements mode appears in the inset in Figure 3. Analysis of the scattering data was done by xPolar software.

3. RESULTS AND DISCUSSION

3.1. Synchrotron X-ray Scattering. *3.1.1. In Situ WAXS Measurements.* We first measured the crystallization profiles, as a function of time, in samples printed along either the short or the long axis, as shown in Figure 1. The 3D printer was placed in the beamline where the beam and the thermal infrared camera were positioned as shown in Figure 1, which enabled us to monitor in situ the evolution of the crystalline structure and correlate it with the temperature profile measured using a high-resolution infrared thermal camera. The temperature profile at the beam spot (labeled with the +) is plotted as a function of time in Figure 4 for samples printed in both orientations. In both cases, the graph starts from 10 s to eliminate imaging artifacts due to fluctuations caused by the proximity of the printing nozzle to the measured point. From the figure, we can see that the rate of cooling is significantly faster for samples printed in the direction perpendicular to the beam. The cooling rate of the structures involves a competition

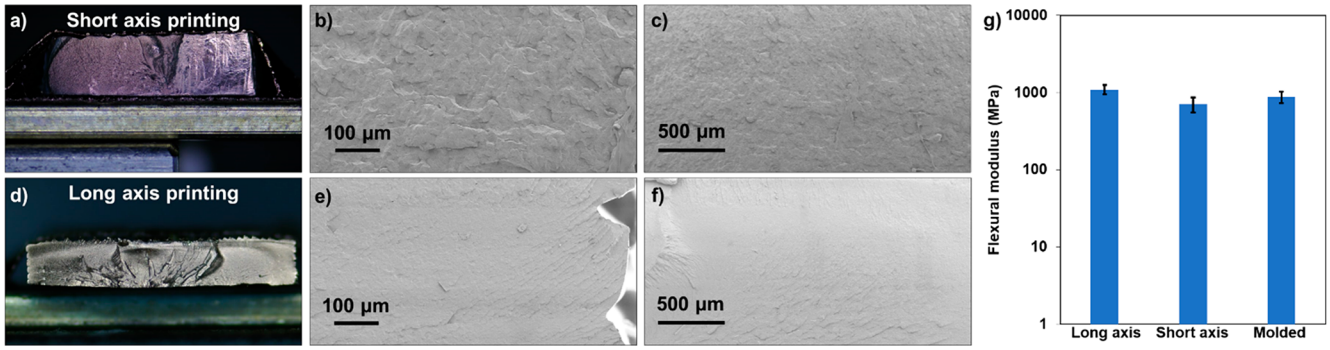

Figure 5. Short axis printed iPP structure: (a) optical image, (b,c) SEM images. Long axis printed iPP structure: (d) optical image, (e,f) SEM images. (g) Flexural modulii by three-point bending.

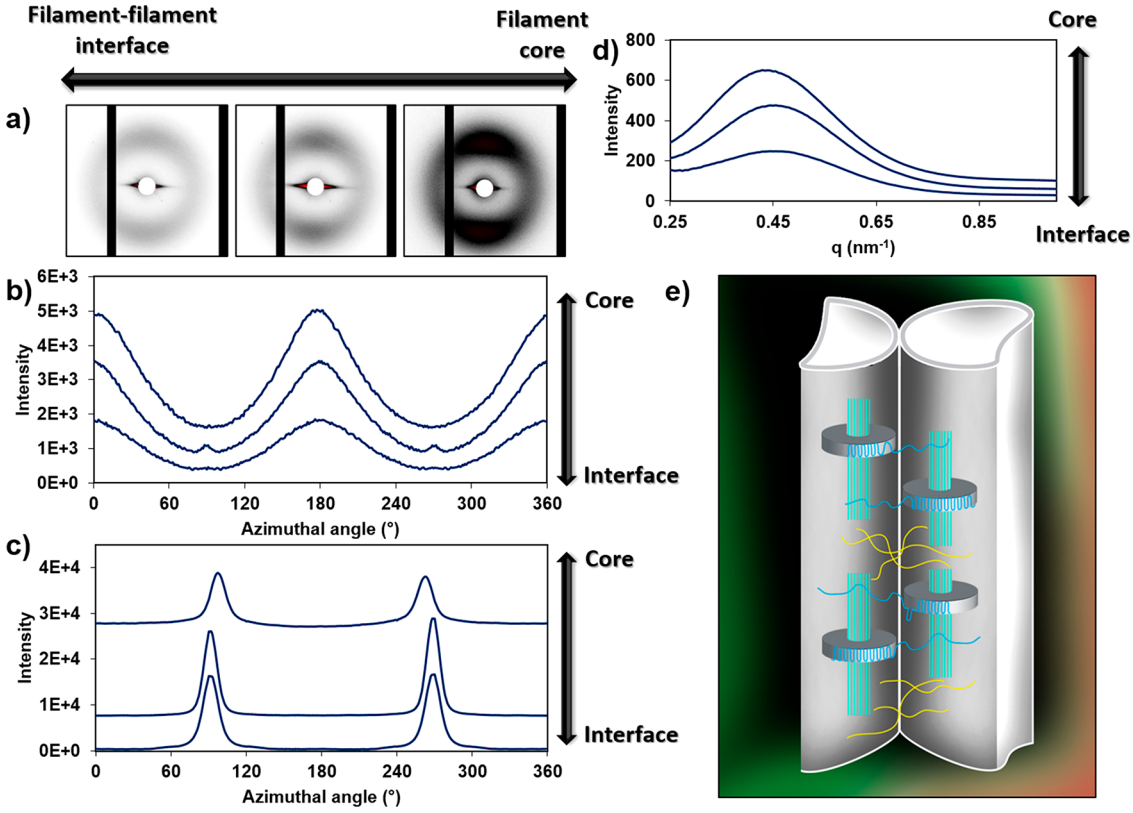

Figure 6. (a) SAXS 2D patterns of microbeam radial scan of iPP from interface to the core. (b) Azimuthal scan for kebab peak for the different radial locations. (c) Azimuthal scan for shish peak for the different radial locations. (d) Corresponding integrated 1D curves for the SAXS 2D patterns. (e) An illustration of structural changes at the interface between two adjacent filaments, showing the remaining aligned shish chains (in green); the interdiffusing of unfolding kebab chains (in blue) and of amorphous chains by reptation (yellow).

between radiative heat loss from the filament surfaces with heat input from the moving nozzle. Initially, the thermal profiles at the "+" are dominated by the proximity of the nozzle. In the parallel orientation, the nozzle moves along the filament axis during deposition, crossing the measured spot only once per deposited layer, while in the perpendicular orientation the nozzle crosses five times during deposition of the same layer. Hence, the temperature at the spot is higher. After about 12 s, the thermal influence of the moving nozzle decreases and the heat loss from the perpendicular orientation becomes higher due to the larger exposed area. Hence, the rate of heat loss is significantly faster in the perpendicular orientation than in the parallel one. As compared to the WAXS scans, we find that the onset of crystallization for the perpendicular orientation was obtained at 121 °C, 42 s after initiating deposition of the filament, and the crystallinity continued to increase, reaching it maximum value 12 s later at a temperature of 109.3 °C. The onset of crystallization in the sample printed in the parallel occurred at the same temperature T = 120.0 °C, but this temperature was reached 60 s from the deposition, and 20 s later the sample reached a temperature of T = 107.5 °C. The 2D WAXS patterns obtained at different intervals are also plotted in the figure. It should be noted that the azimuthal scans of the 040 and 110 WAXS diffraction rings in Figure 4, while showing a notably developed crystallinity, do not provide evidence of preferential orientation, nor do they indicate the existence of daughter lamellae, which are frequently identified by the presence of near meridional 110 diffraction arcs.[23] A similar difference in the thermal profile was also reported previously using a PLA filament.[27] In that case, large

differences in crystal structure were associated with the different thermal profiles, where the samples printed in the parallel orientation exhibited nearly 3 times the degree of crystallinity and had superior mechanical properties, and where it was argued that the longer cooling time also allowed polymer chain migration across interfaces, strengthening the printed product. In the case of iPP, although we can easily see that the final degree of crystallization remains the same for both orientations, in Figure 5 we show SEM images of flexural modulii of the iPP samples printed in the two directions and compared to molded sample, where we can see that no difference with orientation is observed, and even more importantly, no significant difference is observed between the printed and molded samples. The mechanical properties of the printed samples are determined by the ability of the filaments to fuse, and hence the similarity between the molded and printed samples indicates that nearly complete fusion has occurred following printing.

As was discussed previously by McIlroy et al.,[28] good adhesion occurs when the polymer chains can diffuse between the filament interfaces a distance of at least R_g. In the case of PLA, where the self-diffusion coefficient was measured as $D \approx 40 \times 10^{-15}$ cm^2/s, we showed that this condition was met only at elevated nozzle temperatures, where the sample temperature was greater than the PLA melting temperature, T_m = 150 °C. To compare the two systems, we can also estimate the interdiffusion distance, which occurs in the iPP MatEx constructs after deposition of the filament. Gell et al. measured the diffusion coefficient of polypropylene in its entangled melt state using forward recoil spectroscopy.[29] They fitted their results following the WLF equation: $-\log\frac{\eta_0(T)}{\eta_0(T_0)} = \frac{C_1(T-T_0)}{C_2+(T-T_0)}$, where at T_0, C_1 = 6.64, C_2 = 130.4, and $D = 5.1 \times 10^{-15}$ cm^2/s for polypropylene of *Mw* 181 000, with the diffusion coefficient versus the molecular weight given by $D = 1.6 \times 10^{-3}$ M$^{-2.2}$. The diffusion coefficient as a function of temperature for the iPP used in this work with *Mw* = 250 000 was estimated using their work.[29] Using the temperature profile shown in Figure 4, we can then integrate to find the net diffusion length in the relevant temperature range at the points shown for the perpendicular and parallel orientation, to obtain 813 and 517 nm for the parallel and perpendicular orientations, respectively. These values are much larger than R_g, and hence complete fusion is expected before the onset of crystallization. To determine the spatial distribution of the crystallization once cooling initiates, we used micrometer size X-ray beam analysis to scan and map the morphological behavior in the deposited and fused filament.

In the case of PLA, it was shown that interdiffusion was determined by the migration time before the onset of crystallization. In the case of iPP, the degree of crystallization is much higher, and therefore to understand filament−filament fusion, we used an X-ray microbeam to profile the filament, before, during, and after printing.

3.1.2. Macrostructure Variation in the Printed Structure Using Microbeam SAXS. To determine the nature of the crystalline structure and its degree of uniformity across a single filament, samples were first analyzed post printing using a focused microbeam to detect spatial variation. Figure 6a shows 2D patterns of the SAXS scattering for iPP as a function of the radial position in a printed structure. At the core, the iPP exhibits a sharp, long equatorial streak and a circular lobe, which is characteristic of the immature shish-kebab crystalline structure. Shish-kebab structures were previously observed to form in situ following the extrusion process in iPP,[5,6,30,31] and were shown to be a result of chain stretching and orientation. This finding indicates that the shear imposed by the nozzle in the 3D MatEx printing process is sufficiently high to impose the necessary chain stretching and orientation required for the formation of the shish-kebabs.

From Figure 6, we also clearly see that the shish-kebab structure is strongest at the core of the filament and weakens toward the filament−filament interface. In Figure 6b and c, we show the azimuthal scans of the kebab and the shish peaks, respectively, for the three different locations, and in Figure 6d we show the 1D integration curves of the 2D patterns from the center line of the filament to the interface or the area near the adjacent printed filament. From the figure, we can clearly see that the degree of crystallinity and the kebab orientation are highest at the core of the filament and gradually decrease toward the interface region.

Because interdiffusion between filaments is hampered by crystallization, its disappearance in the interfacial region between filaments is advantageous, allowing longer times for interface formation (as illustrated in Figure 6e), and may explain the excellent fusion observed in the SEM images. The existence of this effect though is surprising. Even though the effect can be caused by differences in thermal conductivity, where the interfacial region may cool faster, thermal measurements show that gradients across a single filament are too small to produce a significant effect on the time or rate of crystallization, and hence explain these observations. We therefore explored this effect in greater depth by performing time-resolved measurements with a micrometer size X-ray beam.

3.1.3. Time-Resolved Morphological Variance for Radial Location at the Time of Printing. To better understand the internal structures, which give rise to the large gradients in crystallinity across the iPP filaments, the printing process was monitored in situ using a micro X-ray beam focused at a specific radial location, together with the infrared thermal camera. In this manner, we were able to monitor the time evolution of the internal crystalline morphology across the filament as it is being printed. A cartoon showing the geometrical configuration is shown in Figure 7 together with the thermal image and plot of the temperature versus time in the core and shell regions. From the figure, we can clearly see that no significant difference exists in the thermal retention between these two regions, as mentioned previously. In Figure 8, we show the SAXS patterns. The spectra from three regions, the inner filament core, the shell at the filament surface and interface with the next filament, and a region close to the shell, are shown, but not directly at the interface. From the figure, we can see a clear kebab circular lobe forms first in the SAXS spectrum only at the surface after 12 s from the start of the filament printing. The intensity of the peak increases at 16 s, when faint peaks first appear in the mid and core regions. At 18 s, the peaks in the core and mid sections intensify, while the peak in the shell area weakens. After 30 s, the peak at the core is very intense, the peak in the intermediate region is weaker, and the peak at the filament−filament interface is weakest. The meridional peak appears earliest as well at the shell region, followed by the appearance in the midsection and last in the core. This peak, which corresponds to the shish component, appears to have higher stability against dissolution in time. From the thermal images, we find that the core and outer

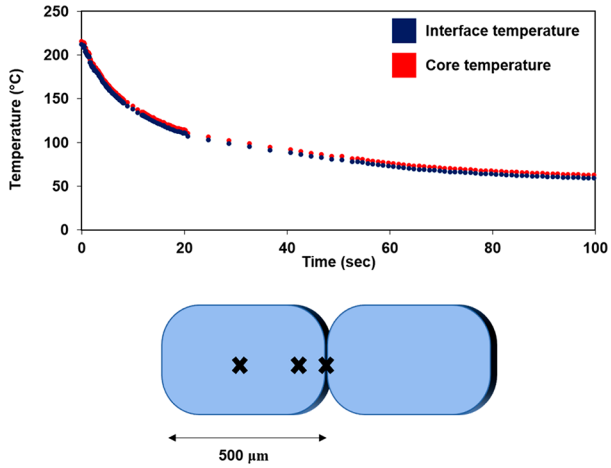

Figure 7. Top: Temperature profiles obtained at the core of a single filament and at the interface between two filaments. Bottom: Schematic description of the filament structures and the position (marked with "×") where X-ray scattering measurements were obtained using the X-ray microbeam.

regions cool at nearly the same rate and hence do not differ significantly in thermal retention, and hence this effect can not be responsible for the differences in crystallization. In fact, as expected, the appearance of the shish-kebab structure occurs first in the shell, where the shear from the nozzle is largest. The orientation is propagated toward the core, which is crystallizing at a slower rate. Yet, in contrast to extrusion of a single filament, something happens to the filament near the interface with the adjacent filament to destabilize the crystalline structures that were just formed. This type of behavior appears to be unique to 3D printing and is very different from the single filament extrusion geometries reported in the literature where the shish-kebab orientation was studied. In 3D printing, the nozzle extrudes filaments, while at the same time producing filament–filament interfaces. Hence, two competing effects act on the filament, initially enhanced crystallization and orientation, which nucleates the shish-kebab structure at the nozzle interface where the shear is highest. The crystalline orientation then propagates more slowly into the interior of the filament. Yet, at the same time, the nozzle also deposits a second filament, which creates an interfacial region with additional free volume that does not exist in the interior. This promotes chain relaxation, and because the temperature isabove T_g for iPP, the chains are very mobile. The mass flow between the adjacent filaments provides a powerful diffusive field, which is enhanced by relaxation of the chains across the interface, unravelling the shish-kebab structures, as shown in Figure 8. In this figure, it is further postulated that the kebab structures are easier to unravel because they are already oriented perpendicular to the interfaces. The shish component is extended parallel to the interface, and hence more difficult to unravel and orient, as evidenced by the greater stability of the azimuthal component in the SAXS spectra.

In Figures 9 and 10, we show the time-resolved X-ray scattering patterns from the medium-angle (MAXS) and wide-angle (WAXS) detectors. In this case as well, we first find the appearance of crystalline peaks after 12 s at the interfacial region corresponding to the alpha crystalline phase. The peaks are visible in both WAXS and MAXS spectra, but with increasing time, starting at 16 s the intensity weakens while the intensity of the MAXS and WAXS peaks from the core appear and continue to grow such that at 30 s, very strong well-

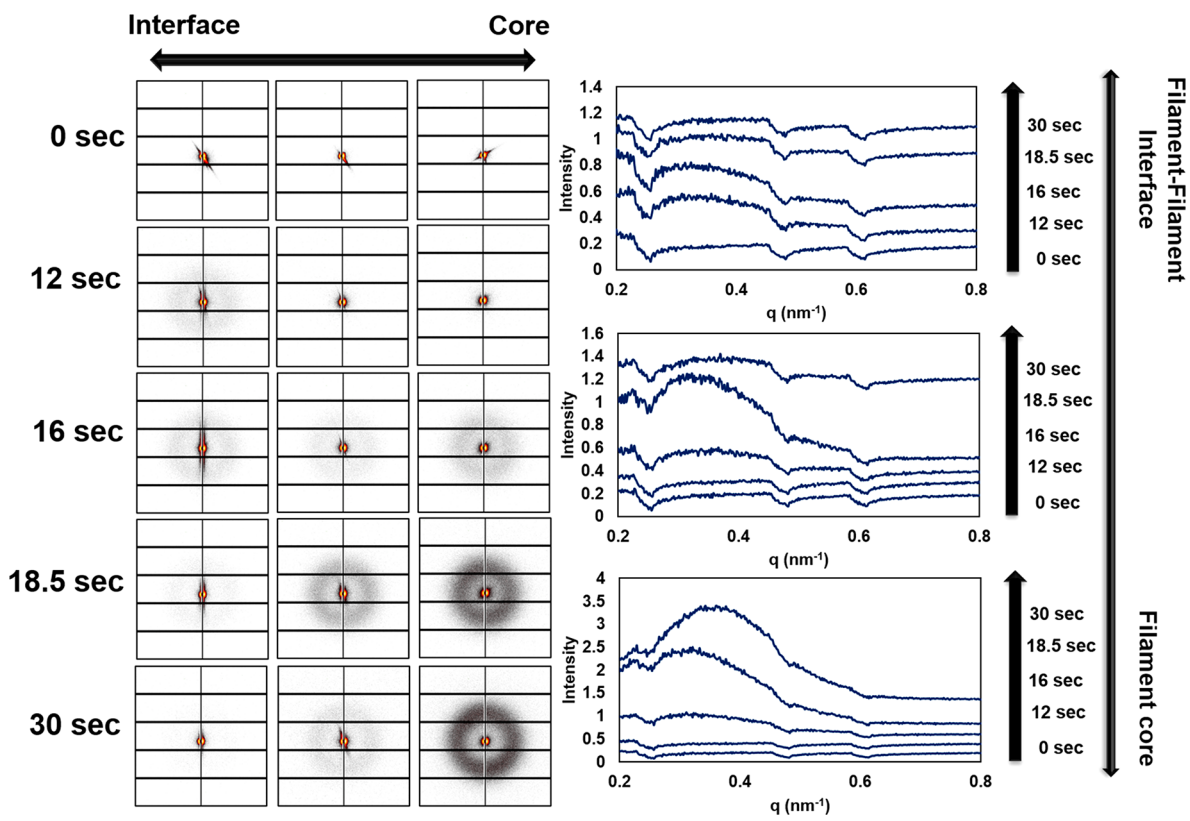

Figure 8. Small-angle X-ray scattering (SAXS) 2D patterns of iPP and the correlated 1D curves as a function of time and radial location.

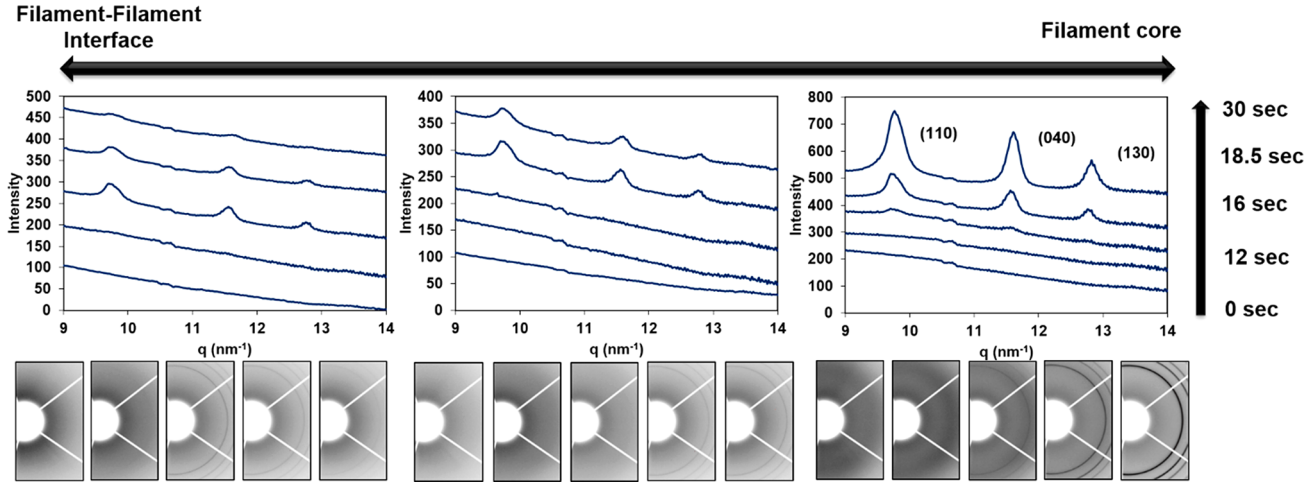

Figure 9. Medium-angle X-ray scattering (MAXS) 2D patterns and the correlated 1D curves as a function of time and radial location.

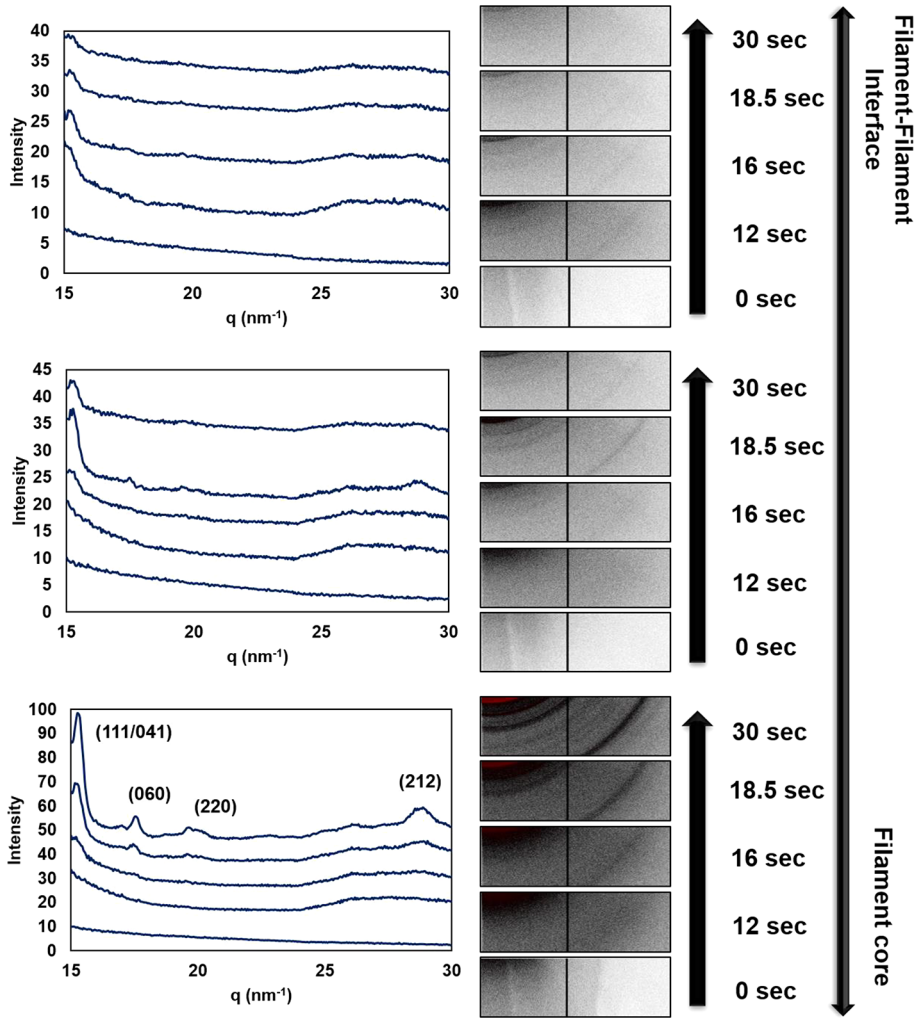

Figure 10. Wide-angle X-ray scattering (WAXS) 2D patterns and the correlated 1D curves as a function of time and radial location.

defined peaks are established in the core, and only a very faint record of the initial peaks in the interfacial regions remains. This behavior is consistent with the SAXS spectra described previously. The data show that the crystalline structure, mostly in the kebab features, unravels in time, but not just at the lamellar region. These data show that the interchain oriented structure also unravels, a fact that is consistent with chain relaxation and possible interfacial diffusion. This behavior is also consistent with the inter filament fusion shown in in the SEM images above, where, in contrast to PLA, the interfacial regions between filaments have disappeared. In Figure 5, we show three-point bending measurements of the flexural

modulii of samples printed in two orientations and molded from virgin polymers. Previously we had shown that for PLA, differences in thermal retention produced large differences in interfilaments fusion, which were then correlated with poor mechanical performance of the printed structures. Here, we find no significant difference between printed structures, regardless of the printing direction, and molded structures, consistent with complete interdiffusion of filaments. Unusual enhancement of the flexural modulii of iPP extruded sheets was also recently reported by Mi et al.[32] They found that building iPP structures via multiple extrusion passes supported on a molded core produced sheets that were much stronger than those extruded or molded in a single pass. SAXS spectra indicated that, while the molded core has standard iPP lamellar spherulites, extrusion caused shish-kebab structures to form on the extruded layers, and SEM images indicated very good fusion between layers. We hypothesize, therefore, that this phenomenon may be of a general nature. Further analysis of the sheets with X-ray microbeams may reveal similar dissociation of the kebabs at the interface, resulting in interfacial fusion similar to that produced in MatEx printing.

4. CONCLUSIONS

We have designed an apparatus, which can be placed directly in an X-ray scattering beamline to simultaneously measure temperature, and SAXS, MAXS, and WAXS spectra with micrometer resolution in situ during MatEx 3D printing. We show how the technique allows us to profile the internal structures of filaments while they are being deposited, and correlate the results with subsequent mechanical measurements. The apparatus was applied to structures printed with isotactic polypropylene, where we found that the high shear of the nozzle resulted in the formation of shish-kebab structures in the filaments after extrusion. The nature of the equilibrium and the time-resolved structures depended on the location of the filament and varied greatly between the core and the interfacial region. X-ray data showed that the shish-kebab structures nucleated first at the surface (shell) of the filaments and propagated inward toward the core. When the second filament was printed, chain relaxation and diffusion occurred across the interface, resulting in nearly complete fusion of the filaments. Three-point-bending measurements of the flexural modulii indicated that there was no significant difference between molded and printed samples, consistent with SEM images of cryo-fractured sample surfaces.

■ ACKNOWLEDGMENTS

We acknowledge support from the National Science Foundation (Inspire Award #1344267) and from the Casali Foundation Israel. We thank Dr. Ellen Wachtel (Weizmann Institute of Science) for insightful discussions on X-ray scattering analysis. WAXS measurements were performed at the 12-BM beamline of the Advanced Photon Source at Argonne National Laboratory, a U.S. Department of Energy (DOE) Office of Science User Facility operated for the DOE Office of Science by Argonne National Laboratory under contract DE-AC02-06CH11357. This research used the SMI beamline (12-ID) of the National Synchrotron Light Source II, a U.S. Department of Energy (DOE) Office of Science User Facility operated for the DOE Office of Science by Brookhaven National Laboratory under contract no. DE-SC0012704. This research used resources of the Advanced Photon Source, a U.S. Department of Energy (DOE) Office of Science User Facility operated for the DOE Office of Science by Argonne National Laboratory under contract no. DE-AC02-06CH11357. This project was supported by grant 9 P41 GM103622 from the National Institute of General Medical Sciences of the National Institutes of Health. The content is solely the responsibility of the authors and does not necessarily reflect the official views of the National Institute of General Medical Sciences or the National Institutes of Health.

■ REFERENCES

(1) Crump, S. S. Apparatus and Method for Creating Three-Dimensional Objects. U.S. Patent 5,121,329, Jun 9, 1992.

(2) Levenhagen, N. P.; Dadmun, M. D. Bimodal Molecular Weight Samples Improve the Isotropy of 3D Printed Polymeric Samples. *Polymer* **2017**, *122*, 232−241.

(3) Peng, F.; Zhao, Z. Y.; Xia, X. H.; Cakmak, M.; Vogt, B. D. Enhanced Impact Resistance of Three-Dimensional-Printed Parts with Structured Filaments. *ACS Appl. Mater. Interfaces* **2018**, *10* (18), 16087−16094.

(4) Seppala, J. E.; Han, S. H.; Hillgartner, K. E.; Davis, C. S.; Migler, K. B. Weld Formation During Material Extrusion Additive Manufacturing. *Soft Matter* **2017**, *13* (38), 6761−6769.

(5) Dikovsky, D.; Marom, G.; Avila-Orta, C. A.; Somani, R. H.; Hsiao, B. S. Shear-Induced Crystallization in Isotactic Polypropylene Containing Ultra-High Molecular Weight Polyethylene Oriented Precursor Domains. *Polymer* **2005**, *46* (9), 3096−3104.

(6) Somani, R. H.; Yang, L.; Hsiao, B. S.; Sun, T.; Pogodina, N. V.; Lustiger, A. Shear-Induced Molecular Orientation and Crystallization in Isotactic Polypropylene: Effects of the Deformation Rate and Strain. *Macromolecules* **2005**, *38* (4), 1244−1255.

(7) Tribout, C.; Monasse, B.; Haudin, J. M. Experimental Study of Shear-Induced Crystallization of an Impact Polypropylene Copolymer. *Colloid Polym. Sci.* **1996**, *274* (3), 197−208.

(8) Peterlin, A. Crystalline Character in Polymers. *J. Polym. Sci., Part C: Polym. Symp.* **1965**, *9* (9), 61−89.

(9) Pennings, A.; Kiel, A. Fractionation of Polymers by Crystallization from Solution, III. On the Morphology of Fibrillar Polyethylene Crystals Grown in Solution. *Colloid Polym. Sci.* **1965**, *205* (2), 160−162.

(10) Hill, M.; Keller, A. Direct Evidence for Distinctive, Stress-Induced Nucleus Crystals in the Crystallization of Oriented Polymer Melts. *J. Macromol. Sci., Part B: Phys.* **1969**, *3* (1), 153−169.

(11) Hill, M.; Keller, A. Further Studies on Polyethylene Crystallized Under Stress: Morphology, Calorimetry, and Stress Relaxation. *J. Macromol. Sci., Part B: Phys.* **1971**, *5* (3), 591−615.

(12) Mackley, M. R.; Keller, A. Flow Induced Crystallization of Polyethylene Melts. *Polymer* **1973**, *14* (1), 16−20.

(13) Janeschitz-Kriegl, H.; Ratajski, E.; Stadlbauer, M. Flow as an Effective Promotor of Nucleation in Polymer Melts: A Quantitative Evaluation. *Rheol. Acta* **2003**, *42* (4), 355−364.

(14) Jerschow, P.; Janeschitz-Kriegl, H. The Role of Long Molecules and Nucleating Agents in Shear Induced Crystallization of Isotactic Polypropylenes. *Int. Polym. Process.* **1997**, *12* (1), 72−77.

(15) Liedauer, S.; Eder, G.; Janeschitz-Kriegl, H.; Jerschow, P.; Geymayer, W.; Ingolic, E. On the Kinetics of Shear Induced

Crystallization in Polypropylene. *Int. Polym. Process.* **1993**, *8* (3), 236–244.
(16) Kumaraswamy, G.; Issaian, A. M.; Kornfield, J. A. Shear-Enhanced Crystallization in Isotactic Polypropylene. 1. Correspondence between In Situ Rheo-Optics and Ex Situ Structure Determination. *Macromolecules* **1999**, *32* (22), 7537–7547.
(17) Kumaraswamy, G.; Verma, R. K.; Issaian, A. M.; Wang, P.; Kornfield, J. A.; Yeh, F.; Hsiao, B. S.; Olley, R. H. Shear-Enhanced Crystallization in Isotactic Polypropylene Part 2. Analysis of the Formation of the Oriented "Skin. *Polymer* **2000**, *41* (25), 8931–8940.
(18) Kumaraswamy, G.; Verma, R. K.; Kornfield, J. A.; Yeh, F. J.; Hsiao, B. S. Shear-Enhanced Crystallization in Isotactic Polypropylene. In-Situ Synchrotron SAXS and WAXD. *Macromolecules* **2004**, *37* (24), 9005–9017.
(19) Seki, M.; Thurman, D. W.; Oberhauser, J. P.; Kornfield, J. A. Shear-Mediated Crystallization of Isotactic Polypropylene: The Role of Long Chain-Long Chain Overlap. *Macromolecules* **2002**, *35* (7), 2583–2594.
(20) Larin, B.; Avila-Orta, C. A.; Somani, R. H.; Hsiao, B. S.; Marom, G. Combined Effect of Shear and Fibrous Fillers on Orientation-Induced Crystallization in Discontinuous Aramid Fiber/Isotactic Polypropylene Composites. *Polymer* **2008**, *49* (1), 295–302.
(21) Larin, B.; Marom, G.; Avila-Orta, C. A.; Somani, R. H.; Hsiao, B. S. Orientated Crystallization in Discontinuous Aramid Fiber/Isotactic Polypropylene Composites Under Shear Flow Conditions. *J. Appl. Polym. Sci.* **2005**, *98* (3), 1113–1118.
(22) Somani, R. H.; Hsiao, B. S.; Nogales, A.; Srinivas, S.; Tsou, A. H.; Sics, I.; Balta-Calleja, F. J.; Ezquerra, T. A. Structure Development During Shear Flow-Induced Crystallization of i-PP: In-Situ Small-Angle X-Ray Scattering Study. *Macromolecules* **2000**, *33* (25), 9385–9394.
(23) Shalom, Y.; Wachtel, E.; Marom, G. Restructuring of Confined Crystalline Morphology in the Drawing Process of VGCF-iPP Nanocomposite Filaments. *Polymer* **2018**, *154*, 218–224.
(24) Tanami, G. A.; Wachtel, E.; Marom, G. Crystalline Structure and Thermodynamic Analysis of Ultra-Low Diameter VGCF-Polypropylene Nanocomposite Monofilaments. *Polym. Compos.* **2016**, *37* (6), 1641–1649.
(25) Tsilingiris, P. Comparative Evaluation of the Infrared Transmission of Polymer Films. *Energy Convers. Manage.* **2003**, *44* (18), 2839–2856.
(26) Jiratrakanvong, J.; Shao, J.; Menendez, M.; Li, X.; Li, J.; Ma, W.; Agam, G.; Irving, T., MuscleX: Software Suite for Diffraction X-Ray Imaging V1.13.1; 2018.
(27) Shmueli, Y.; Jiang, J.; Zhou, Y.; Xue, Y.; Chang, C.-C.; Yuan, G.; Satija, S. K.; Lee, S.; Nam, C.-Y.; Kim, T. Simultaneous In-Situ X-Ray Scattering and Infrared Imaging of Polymer Extrusion in Additive Manufacturing. *ACS Appl. Polym. Mater.* **2019**, *1* (6), 1559–1567.
(28) McIlroy, C.; Olmsted, P. D. Disentanglement Effects on Welding Behaviour of Polymer Melts During the Fused-Filament-Fabrication Method for Additive Manufacturing. *Polymer* **2017**, *123*, 376–391.
(29) Gell, C. B.; Graessley, W. W.; Fetters, L. J. Viscoelasticity and Self-Diffusion in Melts of Entangled Linear Polymers. *J. Polym. Sci., Part B: Polym. Phys.* **1997**, *35* (12), 1933–1942.
(30) Avila-Orta, C. A.; Burger, C.; Somani, R.; Yang, L.; Marom, G.; Medellin-Rodriguez, F. J.; Hsiao, B. S. Shear-Induced Crystallization of Isotactic Polypropylene Within the Oriented Scaffold of Non-crystallineUltrahigh Molecular Weight Polyethylene. *Polymer* **2005**, *46* (20), 8859–8871.
(31) Sakurai, T.; Nozue, Y.; Kasahara, T.; Mizunuma, K.; Yamaguchi, N.; Tashiro, K.; Amemiya, Y. Structural Deformation Behavior of Isotactic Polypropylene with Different Molecular Characteristics during Hot Drawing Process. *Polymer* **2005**, *46* (20), 8846–8858.
(32) Mi, D.; Xia, C.; Jin, M.; Wang, F.; Shen, K.; Zhang, J. Quantification of the Effect of Shish-Kebab Structure on the Mechanical Properties of Polypropylene Samples by Controlling Shear Layer Thickness. *Macromolecules* **2016**, *49* (12), 4571–4578.